



Thermal Decomposition Kinetics of Siderite Ore during Magnetization Roasting

Qiang Zhang^{1,3} · Yongsheng Sun^{1,2,3}  · Yuexin Han^{1,2,3} · Peng Gao^{1,2,3} · Yanjun Li^{1,3}

Received: 15 September 2020 / Accepted: 11 March 2021 / Published online: 26 March 2021
© Society for Mining, Metallurgy & Exploration Inc. 2021

Abstract

The non-isothermal magnetization roasting process and isothermal magnetization roasting process of siderite ore were investigated using thermogravimetric (TG) analysis and a real-time infrared gas analyzer. X-ray diffraction (XRD) and scanning electron microscopy (SEM) with energy dispersive spectroscopy (EDS) were used to analyze the characteristics of samples. The results showed that the decomposition degree and decomposition rate of siderite ore were vitally affected by heating rate and roasting temperature. It was determined that A_1 reaction model ($f(\alpha) = 1 - \alpha$) and $A_{3/2}$ reaction model ($f(\alpha) = (3/2)(1 - \alpha)[- \ln(1 - \alpha)]^{1/2}$) were the most probable mechanism function of the non-isothermal decomposition process and isothermal decomposition process, respectively. The phase transformation and decomposition mechanism during the roasting process were evaluated. Siderite decomposed in the process of magnetization roasting, released CO and CO₂, and transformed into strongly magnetic magnetite. The SEM images highlighted that as the decomposition progressed, the structure of roasted samples was destroyed, and an increasing number of cracks and pores emerged on the surface, which is advantageous to the following grinding process.

Keywords Siderite ore · Magnetization roasting · Non-isothermal kinetic · Isothermal kinetic · Reaction mechanism

1 Introduction

With the continuous growth of global demand, the consumption of high-grade iron ore resources is increasing. Thus, increasing attention has been paid to the utilization of refractory iron ore. However, it is difficult to upgrade the iron ore economically and efficiently because of its low iron grade, fine particle size, and complex mineral composition [1–4]. Siderite ore is a typical complex refractory iron ore resource with abundant reserves, but most of it has not been exploited and utilized by reason of the great difficulties in the beneficiation process [5–7].

Nowadays, the process of magnetization roasting followed by low-intensity magnetic separation is one of the most effective ways to realize the beneficiation of siderite ore [8–11]. Yu et al. [12], Zhao et al. [5], and Chun et al. [13] evaluated the effects of magnetization roasting and magnetic separation conditions on iron grade and iron recovery. The research of Celikdemir et al. [14] indicated that siderite cannot be converted into magnetite when heated by microwaves unless in the presence of a thermal auxiliary (sucrose). Sun et al. [15], Zhang et al. [16], and Zhu et al. [17] conducted in situ magnetization roasting experiments on siderite and hematite to study the green magnetization roasting. The reaction mechanism of siderite lump in coal-based direct reduction was investigated by Zhu et al. [18]. In order to further study the magnetization roasting process of siderite, many scholars have carried out kinetic and thermodynamic analysis. Zhang et al. [19] investigated the effect of heating rate on the pyrolysis behavior and kinetic characteristics of siderite. Jagtap et al. [20] and Zakharov and Adonyi [21] evaluated the effect of particle size on the decomposition of siderite. Alkac and Atalay [22] studied the thermal decomposition kinetics of siderite by TG analysis, and obtained the activation energy values of two optimal three-dimensional diffusion reaction models. Gotor et al. [23] studied the thermal decomposition

✉ Yongsheng Sun
yongshengsun@mail.neu.edu.cn

¹ School of Resources and Civil Engineering, Northeastern University, Shenyang 110819, People's Republic of China

² State Key Laboratory of Rolling and Automation, Northeastern University, Shenyang 110819, People's Republic of China

³ National-local Joint Engineering Research Center of High-efficient exploitation technology for Refractory Iron Ore Resources, Shenyang 110819, People's Republic of China

Table 1 Chemical composition analysis of the siderite ore (mass fraction, %)

Composition	TFe	FeO	Al ₂ O ₃	CaO	MgO	P	S	Mn	K	SiO ₂
Content	22.99	19.41	9.94	0.23	1.90	0.04	0.45	0.61	2.45	35.35

kinetics of natural siderite and artificial siderite in vacuum through TG and CRTA analysis. Their results indicated that the thermal decomposition mechanism of artificial siderite conformed to the A₂ reaction model: $G(\alpha) = [-\ln(1 - \alpha)]^{1/2}$, while the thermal decomposition mechanism of natural siderite was consistent with the F₁ reaction model: $G(\alpha) = 1 - (1 - \alpha)^{1/2}$.

However, there are few studies on the magnetization roasting of natural siderite in different thermodynamic processes. In addition, in the actual process of siderite magnetization roasting, the non-isothermal conditions and isothermal conditions are likely to exist simultaneously. Thus, it is of great significance to understand the decomposition kinetics under these two conditions of magnetization roasting. The objective of this study is to study the kinetics of non-isothermal decomposition and isothermal decomposition of siderite ore via TG analysis and real-time infrared gas analyzer. In this paper, we calculated the kinetic parameters, and revealed the mechanisms of magnetization roasting of siderite ore by XRD and SEM-EDS.

2 Materials and Methods

2.1 Materials

The siderite ore used in this study was collected from Shanxi Province, China. After being crushed, it was ground to a particle size less than 0.2 mm. The results of chemical composition analysis and iron phase analysis of the siderite ore are shown in Tables 1 and 2, respectively. The total iron grade (TFe) was analyzed using the titanium (III) chloride reduction potassium dichromate titration method (routine methods). The FeO content was determined using the potassium dichromate titration method. The S content was determined using high frequency combustion with the infrared absorption method. The content of other components was determined using the wavelength dispersive X-ray fluorescence spectrometric method. The iron phase analysis process is shown in Fig. 1 [24].

Table 2 Iron phase analysis of the siderite ore (mass fraction, %)

Iron phase	Fe in siderite	Fe in magnetite	Fe in hematite/limonite	Fe in pyrite	Fe in silicate	Total
Content	15.51	1.31	4.95	0.30	0.92	22.99
Percentage	67.47	5.70	21.53	1.30	4.00	100.00

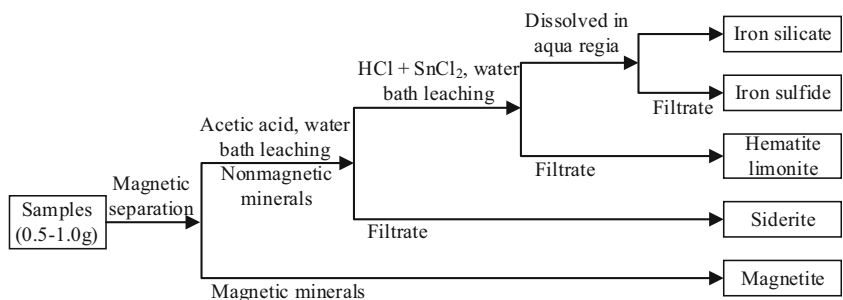
The results in Tables 1 and 2 indicate that the TFe of siderite ore was only 22.99%, and the iron minerals mainly exist in the form of siderite. The contents of P and S were 0.04% and 0.45%, respectively. The low content of MgO (1.90%) and Mn (0.61%) implied that only a small amount of Fe in the siderite lattice was substituted by Mg and Mn. From the chemical composition analysis results in Table 1 and the XRD patterns in Fig. 2, it can be determined that the gangue minerals are mainly quartz and mica. As shown in Fig. 2, the XRD patterns indicated that the main iron ore in the sample is siderite, with a small amount of goethite, and the characteristic diffraction peaks (d-spacing) of siderite are displayed in Table 3. Compared with the literature standard, the characteristic diffraction peaks of siderite in this study shifted to the right and the d-spacing decreased, which may be owing to the isomorphic substitutions of Fe in the structure of siderite by Mg and Mn [25].

2.2 Experimental

The experimental system of this study is shown in Fig. 3. The non-isothermal kinetics magnetization roasting experiments were carried out with a thermal analyzer (SDT Q600; TA instruments, USA). In the non-isothermal roasting experiments, the siderite ore was heated from ambient temperature to 1073.15 K at four different heating rates (5 K min⁻¹, 10 K min⁻¹, 15 K min⁻¹, and 20 K min⁻¹) under nitrogen atmosphere. During the magnetization roasting process, the mass loss and roasting temperature were monitored and recorded simultaneously by a computer connected with the thermal analyzer.

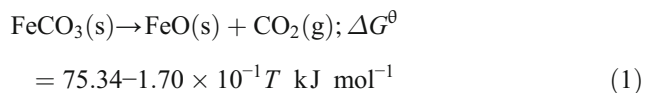
The isothermal roasting experiments were performed in a vertical tube furnace (OTF-1200X-S-VT, Hefei Kejing Materials Technology Co., Ltd., China) with a real-time infrared gas analyzer (Gasboard-3100, Wuhan Sifang Photoelectric Technology Co., Ltd., China). In the isothermal roasting experiments, the furnace was heated from ambient temperature to the predetermined temperatures (823.15 K, 873.15 K, 923.15 K, and 1023.15 K) in nitrogen atmosphere. When the predetermined temperature was reached, the siderite

Fig. 1 Iron phase analysis process



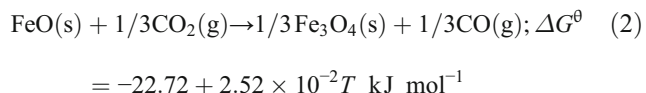
ore sample was introduced into the center of the vertical tube furnace. In the process of magnetization roasting, the concentrations of CO and CO₂ were continuously recorded by a real-time infrared gas analyzer.

During the pyrolysis of siderite in nitrogen atmosphere, the chemical reactions occurred step by step, which can be expressed by Eqs. (1) and (2) [16, 21, 27]:

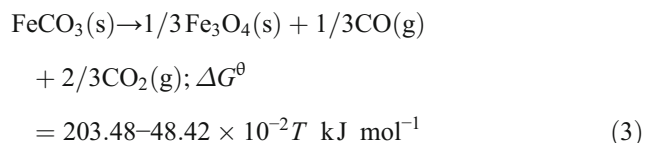


in which ΔG^θ (kJ mol⁻¹) domains the Gibbs free energy and T (K) is the roasting temperature.

As the decomposition product of siderite, wüstite was an unstable intermediate phase, and it can be oxidized by CO₂ to generate CO and magnetite, as shown in Eq. (2).



In the process of siderite decomposition, Eqs. (1) and (2) occurred almost simultaneously. On this basis, the pyrolysis of siderite can be described as:



The phase transformation of siderite ore during the roasting process was investigated by XRD (PW3040, X’Pert PRO, PANalytical, Netherlands) with Cu K α radiation. The morphology of the roasted samples was analyzed by SEM (S-3400 N; Hitachi, Ltd., Tokyo, Japan) equipped with EDS (Oxford INCA energy 300).

2.3 Kinetic Analysis

2.3.1 Non-isothermal Kinetic Data Analysis

The decomposition degree (α) is defined as the ratio of the sample mass loss at a given time t to the sample mass loss at the end of the magnetization roasting process, which is expressed as:

$$\alpha = \frac{W_0 - W_t}{W_0 - W_\infty} \quad (4)$$

Table 3 Characteristic diffraction peaks (d-spacing) of siderite in this paper and the standard d-spacing of siderite in literature

Siderite in this paper		Siderite in literature [26]	
2 θ /°	d-spacing/Å	2 θ /°	Standard d-spacing/Å
24.92	3.5697	24.87	3.5795
32.21	2.7765	32.18	2.7816
38.52	2.3354	38.51	2.3380
42.56	2.1221	42.53	2.1256
46.34	1.9573	46.39	1.9575
50.99	1.7896	51.03	1.7898
53.03	1.7253	52.92	1.7303
61.64	1.5032	60.82	1.5230
65.55	1.4228	65.14	1.4321
68.32	1.3735	68.17	1.3755

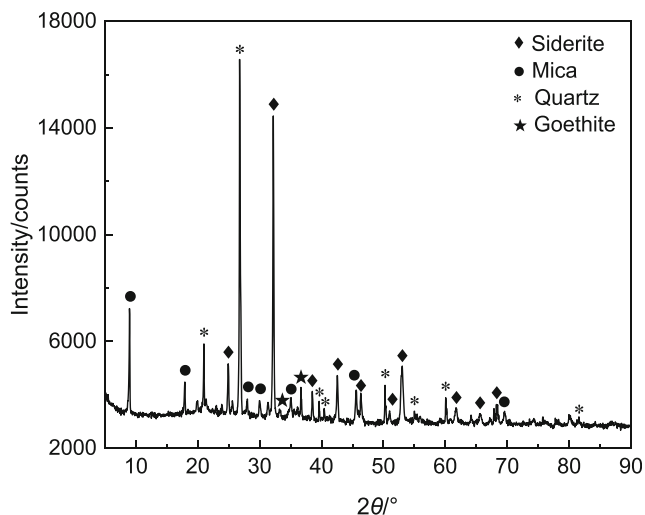
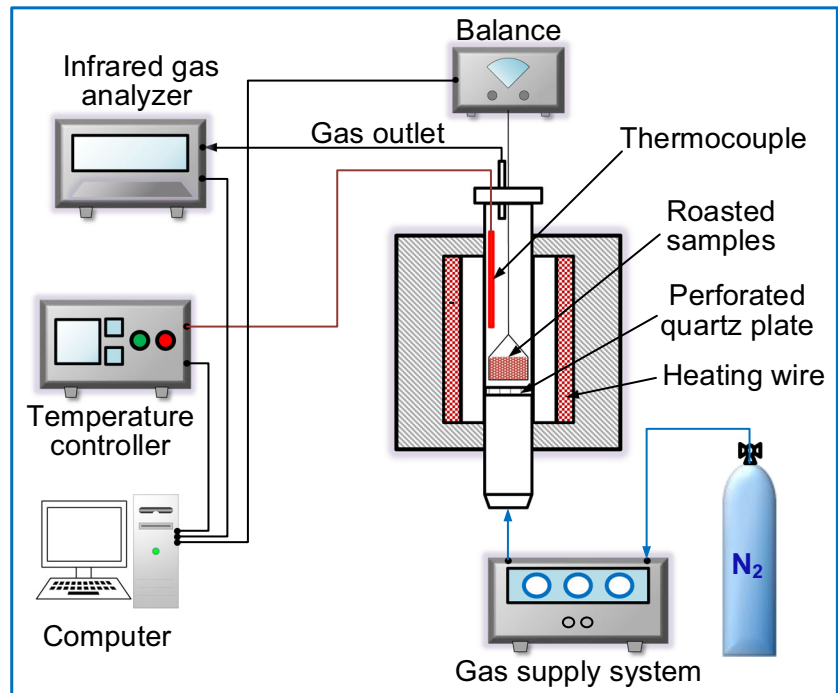


Fig. 2 XRD patterns of the siderite ore

Fig. 3 Schematic diagram of the experimental system



where W_0 (g) is the initial mass of the sample, W_t (g) is the mass of the sample at a given time t , and W_∞ (g) is the mass of the sample at the end of the decomposition.

The decomposition rate (ν , min^{-1}) can be obtained by differentiating the decomposition degree:

$$\nu = \frac{d\alpha}{dt} \tag{5}$$

When the different constant heating rates (β , K min^{-1}) were used for the non-isothermal TG analysis, the decomposition rate of heterogeneous reaction can be expressed as [28]:

$$\frac{d\alpha}{dt} = \beta \frac{d\alpha}{dT} = A \exp\left(\frac{-E}{RT}\right) f(\alpha) \tag{6}$$

in which A is the pre-exponential factor (s^{-1}), E is the apparent activation energy (J mol^{-1}), $f(\alpha)$ is the differential form of mechanism function, and R is the gas constant ($8.314 \text{ J (mol}\cdot\text{K)}^{-1}$).

Table 4 The probable reaction mechanism functions

Mechanism functions	$f(\alpha)$	$G(\alpha)$
A_1	$1 - \alpha$	$-\ln(1-\alpha)$
$A_{3/2}$	$(3/2)(1-\alpha)[- \ln(1-\alpha)]^{1/2}$	$[- \ln(1-\alpha)]^{2/3}$
A_2	$2(1-\alpha)[- \ln(1-\alpha)]^{1/2}$	$[- \ln(1-\alpha)]^{1/2}$
A_3	$3(1-\alpha)[- \ln(1-\alpha)]^{2/3}$	$[- \ln(1-\alpha)]^{1/3}$
A_4	$4(1-\alpha)[- \ln(1-\alpha)]^{3/4}$	$[- \ln(1-\alpha)]^{1/4}$
P_1	$2\alpha^{1/2}$	$\alpha^{1/2}$
P_2	$3\alpha^{1/2}$	$\alpha^{1/3}$
R_1	1	α
R_2	$2(1-\alpha)^{1/2}$	$1-(1-\alpha)^{1/2}$
R_3	$3(1-\alpha)^{2/3}$	$1-(1-\alpha)^{1/3}$
D_1	$1/(2\alpha)$	α^2
D_2	$[- \ln(1-\alpha)]^{-1}$	$\alpha + (1-\alpha)\ln(1-\alpha)$
D_3	$(3/2)(1-\alpha)^{2/3}/[1-(1-\alpha)^{1/3}]$	$[1-(1-\alpha)^{1/3}]^2$
D_4	$(3/2)[(1-\alpha)^{-1/3}-1]^{-1}$	$1-2\alpha/3-(1-\alpha)^{2/3}$
F_0	1	α
F_2	$(1-\alpha)^2$	$(1-\alpha)^{-1}-1$

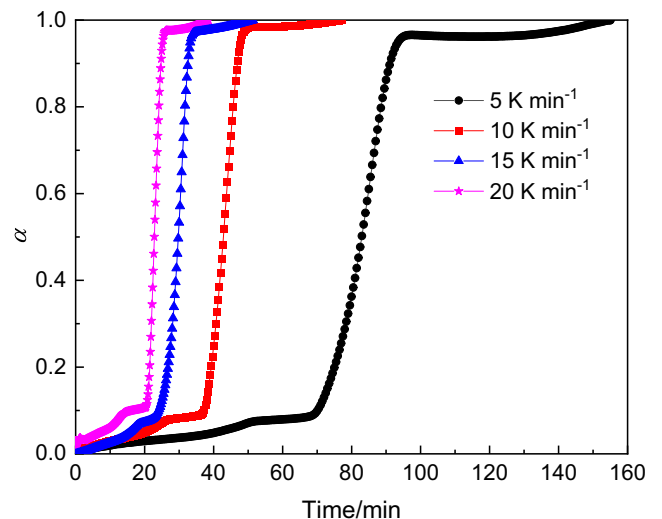


Fig. 4 The decomposition degree (α) versus time at the different heating rates

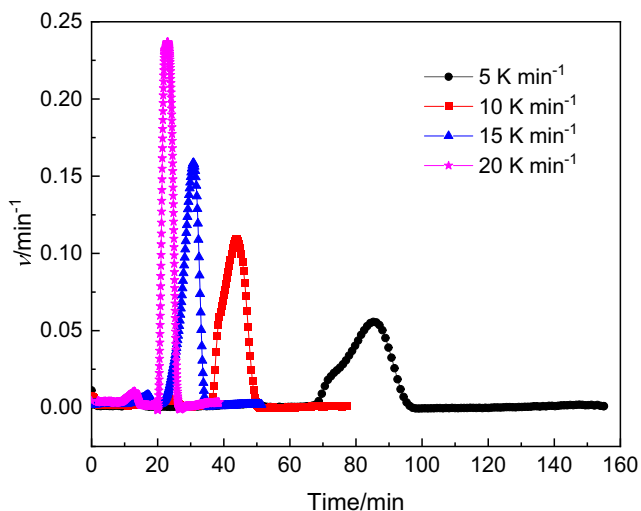


Fig. 5 The decomposition rate (ν) versus time at the different heating rates

Then Eq. (7) can be obtained by rearranging and integrating Eq. (6):

$$G(\alpha) = \int_0^\alpha \frac{d\alpha}{f(\alpha)} = \frac{A}{\beta} \int_{T_0}^T \exp\left(\frac{-E}{RT}\right) dT \quad (7)$$

The Flynn–Wall–Ozawa method is applicable to calculate the apparent activation energy (E) in non-isothermal kinetics [29]:

$$\lg \beta = \lg \left(\frac{AE}{RG(\alpha)} \right) - 2.315 - 0.4567 \frac{E}{RT} \quad (8)$$

where $G(\alpha)$ is the integral form of the mechanism function.

When the same decomposition degree (α) was selected at the different heating rates (β), $G(\alpha)$ was a certain value according to Eq. (5). Therefore, the apparent active energy (E)

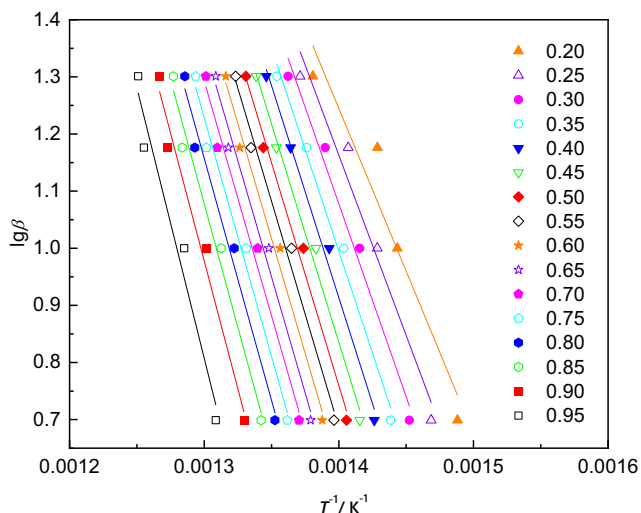


Fig. 6 Linear fitting of $\ln \beta$ versus T^{-1} under non-isothermal conditions

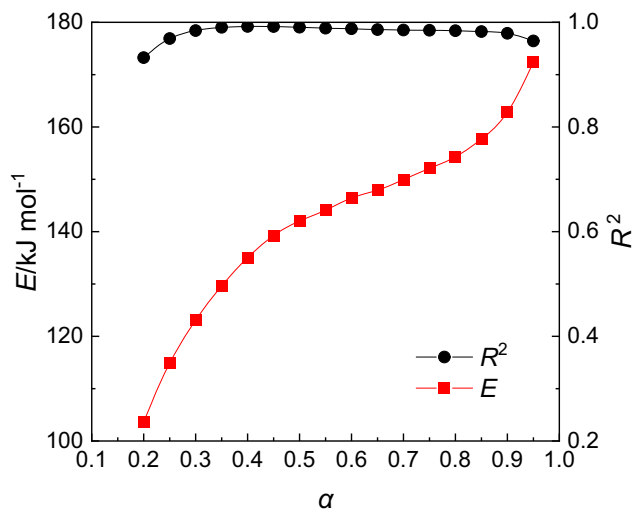


Fig. 7 Calculation results of activation energy based on the Flynn–Wall–Ozawa method

can be obtained from the slope of the linear regression of $\lg \beta$ versus T^{-1} .

In this paper, the integral form of mechanism function $G(\alpha)$ was determined according to the Flynn–Wall–Ozawa method combined with the Šatava–Šesták integral method [30], as shown in Eq. (9):

$$\lg G(\alpha) = \lg \left(\frac{AE_s}{R\beta} \right) - 2.315 - 0.4567 \frac{E_s}{RT} \quad (9)$$

According to the predetermined heating rate (β), the corresponding value of $G(\alpha)$ can be calculated by introducing the decomposition degree (α) into 16 kinds of kinetic mechanism functions shown in Table 4. The apparent activation energy (E_s) and pre-exponential factor (A) can be calculated according to the slope of the linear fitting of $\lg G(\alpha)$ versus T^{-1} . The E_s calculated by the Šatava–Šesták integral method needed to

Table 5 Kinetic parameters of possible mechanism functions based on the Šatava–Šesták method

Mechanism functions	$\beta/\text{K min}^{-1}$	$E_s/\text{kJ mol}^{-1}$	$\ln A/\text{min}^{-1}$	R^2
A_1	5	116.35	17.60	0.9979
	10	128.96	20.03	0.9998
	15	128.96	20.44	0.9998
	20	158.43	24.72	0.9958
$A_{3/2}$	5	77.56	11.37	0.9979
	10	85.97	13.09	0.9998
	15	85.97	13.49	0.9998
	20	105.62	16.38	0.9958
R_3	5	100.39	13.80	0.9982
	10	11,383	16.28	0.9982
	15	113.83	16.69	0.9982
	20	135.20	19.73	0.9862

be compared with E calculated by the Flynn–Wall–Ozawa method to obtain $G(\alpha)$, which satisfied the condition of $|(E - E_s)/E| \leq 1$. By comparing the correlation coefficients (R^2) of each function, the most probable mechanism function was determined, and the non-isothermal kinetic model was established.

2.3.2 Isothermal Kinetic Data Analysis

The decomposition degree (α) in the isothermal roasting experiments can be calculated by Eq. (10).

$$\alpha = \frac{\sum V_t}{\sum V_n} = k(T)f(\alpha) \tag{10}$$

where $\sum V_t(\text{mL})$ is the cumulative volume of gas generated from the beginning to the time t during the magnetization roasting process, $\sum V_n(\text{mL})$ is the cumulative volume of gas produced from the beginning to the end of the magnetization roasting, $k(T)$ is the apparent rate constant at the roasting temperature (T), and $f(\alpha)$ is the differential form of mechanism function that describes the decomposition of siderite ore.

The relationship between $k(T)$, apparent activation energy (E), and pre-exponential factor (A) can be expressed by Arrhenius equation [31]:

$$k(T) = Ae^{-\frac{E}{RT}} \tag{11}$$

Equation (12) was obtained by rearranging and integrating Eq. (11).

$$G(\alpha) = k(T)t \tag{12}$$

Using the mechanism function in Table 4, $G(\alpha)$ versus time t was linear regression fitted. The mechanism function is obtained by comparing the values of correlation coefficients (R^2). The apparent rate constant $k(T)$ corresponding to the different roasting temperatures (T) is introduced into Eq. (12) to calculate the pre-exponential factor (A) and activation energy (E).

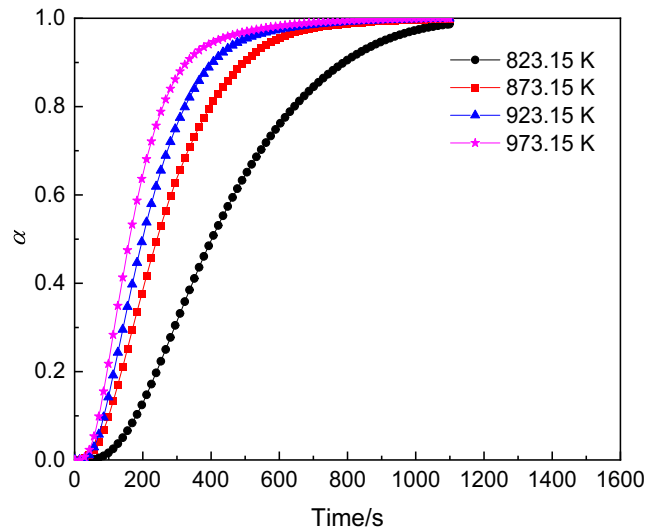


Fig. 8 The decomposition degree (α) versus time at the different roasting temperatures

3 Results and Discussion

3.1 Non-isothermal Decomposition Kinetics

3.1.1 Effects of Heating Rates

In the non-isothermal decomposition experiments, the siderite ore was roasted at four different heating rates (5 K min^{-1} , 10 K min^{-1} , 15 K min^{-1} , and 20 K min^{-1}) from ambient temperature to 1073.15 K . The decomposition degree (α) and decomposition rate (ν) as a function of time t are shown in Figs. 4 and 5, respectively.

As shown in Fig. 4, the siderite ore was almost completely decomposed at the different heating rates. The decomposition process can be divided into three stages, namely induction stage ($\alpha = 0-0.2$), acceleration stage ($\alpha = 0.2-0.9$), and deceleration stage ($\alpha = 0.9-1.0$). In the induction stage, the decomposition of siderite ore began gradually, proceeded rapidly during the acceleration stage, and then gradually slowed down until the end of decomposition. As the heating rate increased from 5 K min^{-1} to 20 K min^{-1} , the time of each decomposition stage gradually decreased. The corresponding roasting time for the decomposition degree to reach 0.9 at the heating rate of 5 K min^{-1} , 10 K min^{-1} , 15 K min^{-1} , and 20 K min^{-1}

Table 6 Non-isothermal decomposition kinetic models of the siderite ore

Mechanism function	$\beta/\text{K min}^{-1}$	Kinetic model
A_1	5	$d\alpha/dT=10329992\exp(-13,994.46716/T)(1-\alpha)$
	10	$d\alpha/dT=49994067\exp(-15,511/T)(1-\alpha)$
	15	$d\alpha/dT=50221300\exp(-15,511/T)(1-\alpha)$
	20	$d\alpha/dT=272100661\exp(-19,055/T)(1-\alpha)$

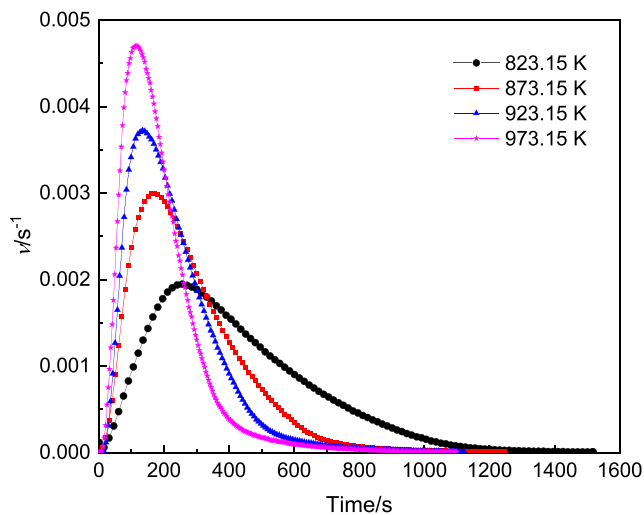


Fig. 9 The decomposition rate (ν) versus time at the different roasting temperatures

min^{-1} was 91.11 min, 46.89 min, 32.55 min, and 24.73 min, respectively (Fig. 4). As can be seen from Fig. 5, with the increase of heating rate, the peak value of decomposition rate increased significantly, and the time to reach the peak value decreased. The peak decomposition rate increased from 0.06 min^{-1} to 0.24 min^{-1} as the heating rate varied from 5 K min^{-1} to 20 K min^{-1} , which indicated that the heating rate influenced the decomposition rate remarkably. Accordingly, the decomposition process can be accomplished in a relatively short time by increasing the heating rate within a certain range.

Table 8 Values of $k(T)$ at the different roasting temperatures

Temperature/ K	823.15	873.15	923.15	973.15
$k(T)/\text{s}^{-1}$	0.00250	0.00333	0.00369	0.00395

3.1.2 Non-isothermal Kinetic Model

In the main decomposition stage of siderite ore ($\alpha = 0.20\text{--}0.95$, increment = 0.05), the roasting temperature (T), the reaction fraction (α), and the heating rate (β) were substituted into Eq. (8) for the linear fitting of $\lg\beta$ and T^{-1} (Fig. 6). From the slopes, the activation energy (E) can be calculated by the Flynn–Wall–Ozawa method. The values of E are presented in Fig. 7, from which it can be seen that the values of E increased from $103.65 \text{ kJ mol}^{-1}$ to $172.40 \text{ kJ mol}^{-1}$, with the values of α increasing from 0.20 to 0.95, and the average value of E was $142.22 \text{ kJ mol}^{-1}$. This indicated that at the initial acceleration stage, the decomposition of siderite proceeded easily with a fast decomposition rate. As the decomposition progressed, the decomposition became more difficult and the decomposition rate decreased. This was consistent with the analysis results in Figs. 4 and 5.

The mechanism function was determined according to the Šatava–Šesták method shown in Eq. (9), and the linearity of $G(\alpha)$ for A_1 , $A_{3/2}$, and R_3 versus T^{-1} was great. The calculated results of the kinetic parameters (activation

Table 7 Linear regression fitting results of $G(\alpha)$ versus t

Mechanism functions	R^2 at different roasting temperature				Average value of R^2
	823.15 K	873.15 K	923.15 K	973.15 K	
A_1	0.9480	0.9796	0.9851	0.9921	0.9762
$A_{3/2}$	0.9944	0.9979	0.9947	0.9893	0.9941
A_2	0.9984	0.9896	0.9823	0.9718	0.9855
A_3	0.9769	0.9606	0.9512	0.9378	0.9566
A_4	0.9511	0.9341	0.9252	0.9118	0.9305
P_1	0.9135	0.8880	0.8788	0.8607	0.8853
P_2	0.8872	0.8655	0.8584	0.8428	0.8635
R_1	0.9515	0.9237	0.9125	0.8913	0.9198
R_2	0.9878	0.9693	0.9601	0.9427	0.9649
R_3	0.9953	0.9865	0.9801	0.9674	0.9823
D_1	0.9715	0.9501	0.9399	0.9195	0.9452
D_2	0.9797	0.9687	0.9619	0.9461	0.9641
D_3	0.9523	0.9831	0.9895	0.9934	0.9796
D_4	0.9800	0.9794	0.9761	0.9652	0.9752
F_0	0.9515	0.9237	0.9125	0.8913	0.9198
F_2	0.0434	0.0517	0.0459	0.0581	0.0498

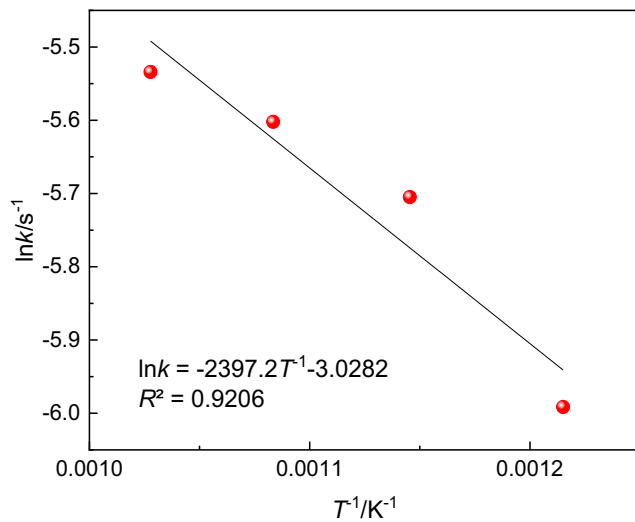
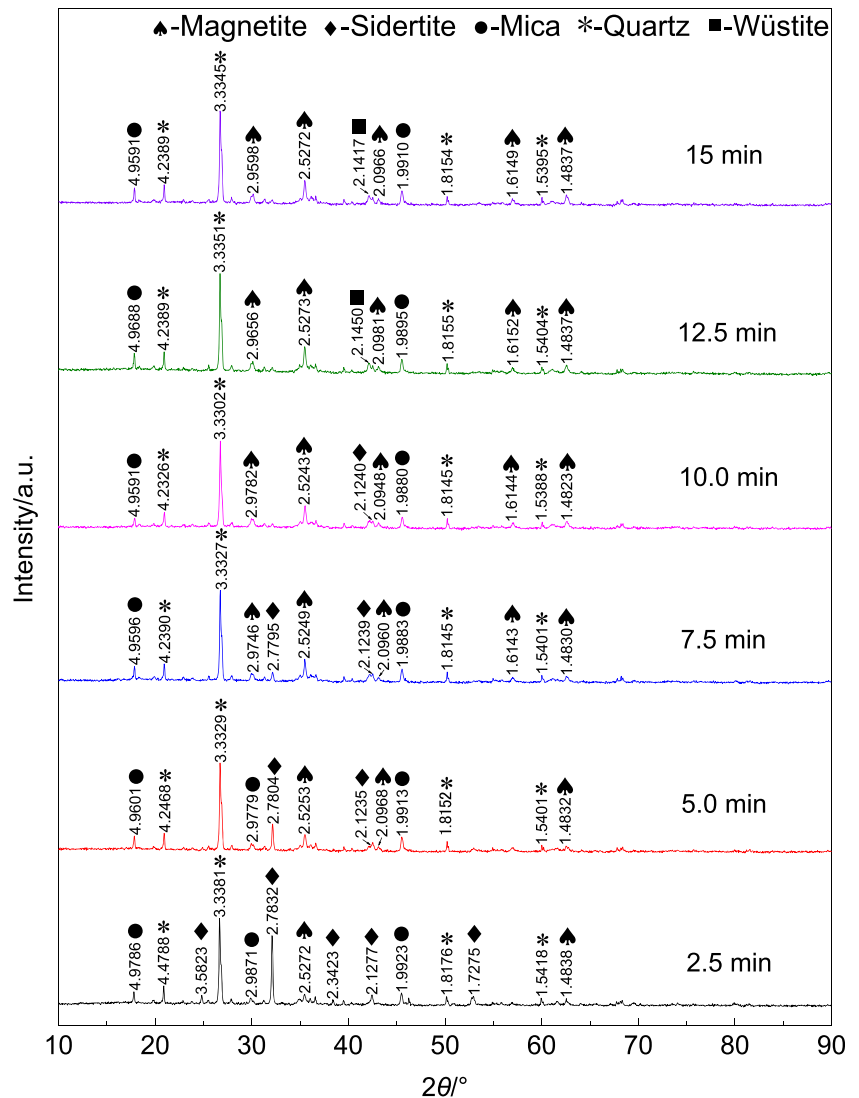


Fig. 10 Linear regression fitting of $\ln k$ versus T^{-1}

energy E_s and pre-exponential factor $\ln A$ of A_1 , $A_{3/2}$, and R_3 reaction models are shown in Table 5. By comparing the activation energies in Fig. 7 and those in Table 5, it can be observed that the activation energies of A_1 reaction model satisfied the relation of $|(E - E_s)/E| \leq 1$. Therefore, A_1 reaction model (Avrami-Erofeev's model, $n = 1$), namely $f(\alpha) = 1 - \alpha$ and $G(\alpha) = -\ln(1 - \alpha)$ was the most probable mechanism function of the non-isothermal decomposition of siderite ore, which was characterized by the formation of solid products accompanied by random nucleation and subsequent grain growth [32]. Nucleation was the first step in the formation of a new phase and the rate control step in the crystal growth process. Using the kinetic parameters (activation energy E_s and pre-exponential factor $\ln A$) and the mechanism function, kinetic models of the non-isothermal decomposition of siderite ore at different heating rates were acquired, as presented in Table 6.

Fig. 11 XRD patterns of samples roasted at 873.15 K with different roasting time



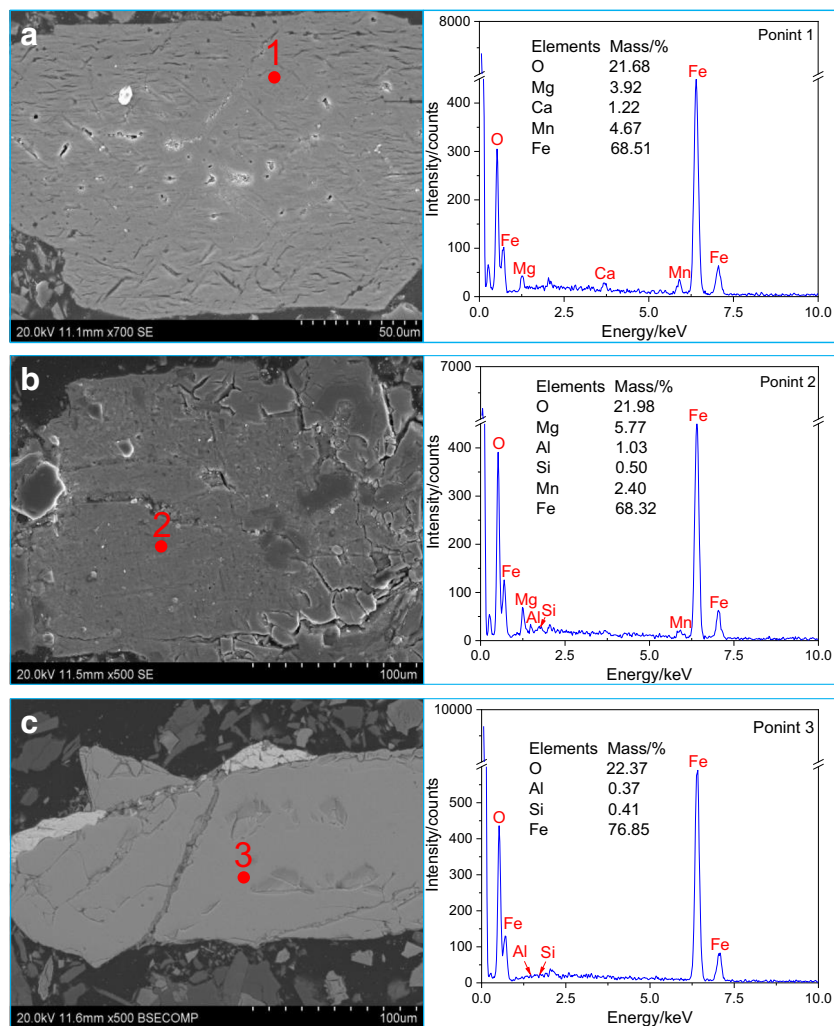


Fig. 12 SEM-EDS analysis results of the roasted samples at the different roasting time (a 2.5 min, b 5 min, c 7.5 min, d 10 min, e 12.5 min, f 15 min)

3.2 Isothermal Decomposition Kinetics

3.2.1 Effect of Roasting Temperature

During the isothermal decomposition experiments, the effect of roasting temperature on the decomposition degree of siderite ore is presented in Fig. 8. The curves shape of the decomposition degree versus time at the different roasting temperatures was similar. The decomposition degree first increased rapidly in the initial stage and then slowly increased with the decomposition proceeding until the end of the decomposition. With the roasting temperature increasing from 823.15 K to 973.15 K, the terminal time of decomposition was gradually shortened.

The decomposition rates at the different roasting temperatures were obtained according to Eq. (5), as presented in Fig. 9. As decomposition proceeded, the decomposition rate increased rapidly before reaching its peak and then decreased rapidly until the end of the decomposition. It can be observed that the decomposition rate reached its peak in a shorter time

with the increase of the roasting temperature, and the maximum decomposition rate was 0.00468 s^{-1} at 973.15 K.

From Figs. 8 and 9, it can be found that increasing the roasting temperature in a certain range can increase the peak value of the decomposition rate and shorten the time required for the decomposition of siderite ore.

3.2.2 Isothermal Kinetic Model

The most probable mechanism function of siderite ore decomposition could be obtained according to the integral method mentioned. It can be seen from Table 7 that $A_{3/2}$ reaction model ($f(\alpha) = (3/2)(1 - \alpha)[- \ln(1 - \alpha)]^{1/2}$ and $G(\alpha) = [- \ln(1 - \alpha)]^{2/3}$) had the best fitting effect by comparing the correlation coefficients (R^2) of each mechanism function. Both non-isothermal kinetic mechanisms and isothermal kinetic mechanisms were random nucleation and growth kinetic models, but the reaction order was different. In the process of siderite decomposition, the nucleation occurred randomly throughout the whole volume and stopped growing at the

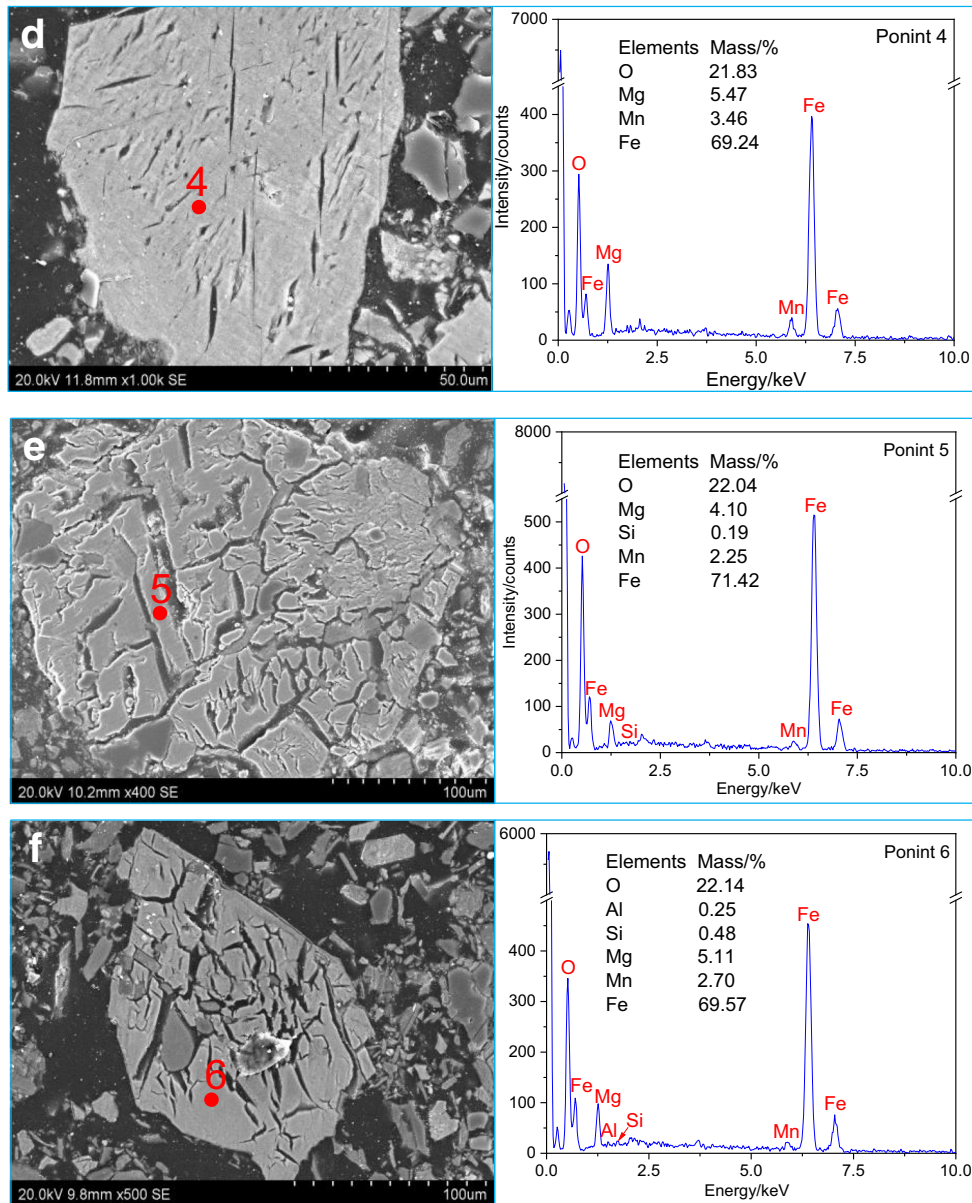


Fig. 12 (continued)

place of impact, and when the growing grains or particles combined with each other, the interfacial area decreased obviously [33].

The reaction rate constant $k(T)$ at the different roasting temperature of $A_{3/2}$ reaction model was obtained by Eq. (12), as shown in Table 8. The linear regression curve of $\ln k$ versus T^{-1} at the different roasting temperatures of $A_{3/2}$ reaction model is shown in Fig. 10. The correlation coefficient (R^2) of $\ln k$ versus T^{-1} was 0.9206, which indicated that the linear correlation between them was great. According to the slope and intercept of the fitting line, the pre-exponential factor (A) and the apparent activation energy (E) were calculated, which were 0.0484 s^{-1} and $19.932 \text{ kJ mol}^{-1}$, respectively.

3.3 Reaction Mechanism Analysis

To explain the mechanism of siderite ore decomposition, the roasted samples at the roasting temperature of 873.15 K for 2.5 min, 5 min, 7.5 min, 10 min, 12.5 min, and 15 min were investigated by XRD and SEM-EDS, as shown in Figs. 11 and 12.

The content of magnetite in the raw samples was very low, and there were no obvious diffraction characteristic peaks of magnetite in the XRD patterns in Fig. 2. The diffraction characteristic peaks (d -spacing = 2.5272 \AA or 1.4838 \AA) of magnetite appeared on the XRD patterns after the sample was roasted for 2.5 min, while the iron mineral in the sample was

still dominated by siderite. With the decomposition proceeding, the number and intensity of the diffraction characteristic peaks of magnetite increased. The decomposition of siderite ore proceeded from the outside to the inside of particles [34]. In a short roasting time, the wüstite formed in the outer layer reacted with CO₂ immediately to form magnetite [27]; thus, there was no characteristic diffraction peak of wüstite in the XRD patterns. As the roasting time increased, siderite inside the particles decomposed. However, since CO₂ was difficult to diffuse inside the particles, wüstite cannot fully react with CO₂. Consequently, when the roasting time reached 10 min, the wüstite diffraction characteristic peak with a d-spacing of 2.1386 Å appeared, while the diffraction characteristic peaks of siderite disappeared. These results indicated that siderite can be self-magnetized in the process of magnetization roasting under nitrogen atmosphere [7].

It can be observed from Fig. 12a that at the beginning of siderite decomposition, the decomposition degree was small and the surface of particles was relatively smooth. The structure of siderite collapsed from the edge of particles with the escape of CO and CO₂ produced in the decomposition process, as shown in Fig. 12b–d. This was because the lattice defects lead to more reaction sites at the edge of particles, which made the decomposition of siderite easier to proceed [16]. As the decomposition progressed, the number of cracks increased, and they connected with each other and extended to the interior of particles. When the decomposition progress was nearly completed, it can be observed from Fig. 12e and f that the particles became loose and porous, which was conducive to the subsequent grinding of roasted products.

4 Conclusion

The non-isothermal magnetization roasting process and isothermal magnetization roasting process of siderite ore was studied. The corresponding kinetic model was determined and the reaction mechanism was explored.

- (1) In the process of non-isothermal magnetization roasting, the decomposition degree and decomposition rate changed with the roasting time in a similar trend under the different heating rates and were influenced by the heating rates significantly. With the increase of heating rate, the decomposition of siderite ore finished in a shorter time. The most probable mechanism function for the non-isothermal decomposition of siderite ore was A₁ reaction model ($f(\alpha) = 1 - \alpha$ and $G(\alpha) = -\ln(1 - \alpha)$). Both the pre-exponential factor and apparent activation energy increased with the increase of heating rate.
- (2) The results of isothermal decomposition indicated that the roasting temperature was an important factor

affecting the siderite decomposition rate. The time required for the decomposition of siderite ore was greatly shortened with the increase of roasting temperature. The optimum mechanism function of isothermal decomposition was A_{3/2} reaction model ($f(\alpha) = (3/2)(1 - \alpha)[- \ln(1 - \alpha)]^{1/2}$ and $G(\alpha) = [- \ln(1 - \alpha)]^{2/3}$), whose pre-exponential factor and apparent activation energy were 0.0484 s⁻¹ and 19.932 kJ mol⁻¹, respectively.

- (3) With the decomposition of siderite ore proceeding, siderite was transformed into the magnetite gradually, while there was no obvious change in the gangue minerals during the decomposition process. The siderite ore structure was destroyed gradually from the edge of particles to its inner core, which was favorable for the following grinding process.

Funding The authors acknowledge the financial support provided by the National Natural Science Foundation of China (Nos. 51874071, 51734005), the Fok Ying Tung Education Foundation for Young Teachers in the Higher Education Institutions of China (No. 161045), and Liao Ning Revitalization Talents Program (XLYC1807111).

Authors' Contribution **Qiang Zhang:** data curation, formal analysis, validation, writing – original draft. **Yongsheng Sun:** conceptualization, funding acquisition, resources, writing – review & editing. **Yuexin Han:** data curation, funding acquisition, project administration, resources. **Peng Gao:** data curation, resources, supervision. **YanJun Li:** Data curation, resources, supervision.

Data Availability Statement The data that support the findings of this study are available from the corresponding author upon reasonable request.

Declarations

Conflict of Interest The authors declare that they have no conflict of interest.

References

1. Sun Y, Han Y, Gao P, Wei X, Li G (2015) Thermogravimetric study of coal-based reduction of oolitic iron ore: kinetics and mechanisms. *Int J Min Process* 143:87–97. <https://doi.org/10.1016/j.minpro.2015.09.005>
2. Zhang X, Han Y, Sun Y, Li Y (2019) Innovative utilization of refractory iron ore via suspension magnetization roasting: a pilot-scale study. *Powder Technol* 352:16–24. <https://doi.org/10.1016/j.powtec.2019.04.042>
3. Sun Y, Gao P, Han Y, Ren D (2013) Reaction behavior of Iron minerals and metallic Iron particles growth in coal-based reduction of an Oolitic Iron ore. *Indust Eng Chem Res* 52(6):2323–2329. <https://doi.org/10.1021/ie303233k>
4. Tang Z, Gao P, Sun Y, Han Y, Li E, Chen J, Zhang Y (2020) Studies on the fluidization performance of a novel fluidized bed reactor for iron ore suspension roasting. *Powder Technol* 360: 649–657. <https://doi.org/10.1016/j.powtec.2019.09.092>

5. Zhao Q, Xue J, Chen W (2019) Upgrading of iron concentrate by fluidized-bed magnetizing roasting of siderite to magnetite in CO–H₂–N₂ atmosphere. *Trans Indian Institute Metals* 72(5):1381–1391. <https://doi.org/10.1007/s12666-019-01636-w>
6. Zhao Q, Xue J, Chen W (2020) Mechanism of improved magnetizing roasting of siderite–hematite iron ore using a synergistic CO–H₂ mixture. *J Iron Steel Res Int* 27(1):12–21. <https://doi.org/10.1007/s42243-019-00242-w>
7. Luo Y, Zhu D, Pan J, Zhou X (2016) Thermal decomposition behaviour and kinetics of Xinjiang siderite ore. *Min Process Extract Metallurgy* 125(1):17–25. <https://doi.org/10.1080/03719553.2015.1118213>
8. Yu J, Han Y, Li Y, Gao P (2017) Beneficiation of an iron ore fines by magnetization roasting and magnetic separation. *Int J Min Process* 168:102–108. <https://doi.org/10.1016/j.minpro.2017.09.012>
9. Yuan S, Zhou W, Han Y, Li Y (2019) Selective enrichment of iron from fine-grained complex limonite using suspension magnetization roasting followed by magnetic separation. *Separation Sci Technol* 55(18):3427–3437. <https://doi.org/10.1080/01496395.2019.1677715>
10. Roy SK, Nayak D, Dash N, Dhawan N, Rath SS (2020) Microwave-assisted reduction roasting—magnetic separation studies of two mineralogically different low-grade iron ores. *Int J Min Metallurgy Mater* 27(11):1449–1461. <https://doi.org/10.1007/s12613-020-1992-5>
11. Li Y, Wang R, Han Y, Wei X (2015) Phase transformation in suspension roasting of oolitic hematite ore. *J Central South Univ* 22(12):4560–4565. <https://doi.org/10.1007/s11771-015-3006-8>
12. Yu J, Han Y, Li Y, Gao P, Sun Y (2017) Separation and recovery of iron from a low-grade carbonate-bearing iron ore using magnetizing roasting followed by magnetic separation. *Separation Sci Technol* 52(10):1768–1774. <https://doi.org/10.1080/01496395.2017.1296867>
13. Chun T, Zhu D, Pan J (2015) Simultaneously roasting and magnetic separation to treat low grade siderite and hematite ores. *Min Process Extract Metallurgy Rev* 36(4):223–226. <https://doi.org/10.1080/08827508.2014.928620>
14. Celikdemir M, Sarikaya M, Depci T, Aydogmus R (2016) Influence of microwave heating and thermal auxiliary on decomposition of siderite. *IOP Conf Ser: Earth Environ Sci* 44:052002. <https://iopscience.iop.org/article/10.1088/1755-1315/44/5/052002>
15. Sun Y, Zhu X, Han Y, Li Y (2019) Green magnetization roasting technology for refractory iron ore using siderite as a reductant. *J Cleaner Product* 206:40–50. <https://doi.org/10.1016/j.jclepro.2018.09.113>
16. Zhang Q, Sun Y, Han Y, Li Y (2020) Pyrolysis behavior of a green and clean reductant for suspension magnetization roasting. *J Cleaner Product* 268:122173. <https://doi.org/10.1016/j.jclepro.2020.122173>
17. Zhu X, Han Y, Sun Y, Li Y, Wang H (2020) Siderite as a novel reductant for clean utilization of refractory iron ore. *J Cleaner Product* 245:118704. <https://doi.org/10.1016/j.jclepro.2019.118704>
18. Zhu D, Luo Y, Pan J, Zhou X (2016) Reaction mechanism of siderite lump in coal-based direct reduction. *High Temp Mater Process* 35(2):185–194. <https://doi.org/10.1515/htmp-2014-0176>
19. Zhang X, Han Y, Li Y, Sun Y (2017) Effect of heating rate on pyrolysis behavior and kinetic characteristics of siderite. *Minerals* 7(11):211. <https://doi.org/10.3390/min7110211>
20. Jagtap S, Pande A, Gokarn A (1992) Kinetics of thermal decomposition of siderite: effect of particle size. *Int J Min Process* 36(1–2): 113–124. [https://doi.org/10.1016/0301-7516\(92\)90068-8](https://doi.org/10.1016/0301-7516(92)90068-8)
21. Zakharov VY, Adonyi Z (1986) Thermal decomposition kinetics of siderite. *Thermochim Acta* 102:101–107. [https://doi.org/10.1016/0040-6031\(86\)85318-7](https://doi.org/10.1016/0040-6031(86)85318-7)
22. Alkac D, Atalay Ü (2008) Kinetics of thermal decomposition of Hekimhan–Deveci siderite ore samples. *Int J Min Process* 87(3–4):120–128. <https://doi.org/10.1016/j.minpro.2008.02.007>
23. Gotor FJ, Macias M, Ortega A, Criado JM (2000) Comparative study of the kinetics of the thermal decomposition of synthetic and natural siderite samples. *Physics Chem Min* 27(7):495–503. <https://doi.org/10.1007/s002690000093>
24. Yuan S, Zhou W, Han Y, Li Y (2020) Selective enrichment of iron from fine-grained complex limonite using suspension magnetization roasting followed by magnetic separation. *Separation Sci Technol* 55(18):3427–3437. <https://doi.org/10.1080/01496395.2019.1677715>
25. Ponomar V, Dudchenko N, Brik A (2017) Phase transformations of siderite ore by the thermomagnetic analysis data. *J Magnetism Magnetic Mater* 423:373–378. <https://doi.org/10.1016/j.jmmm.2016.09.124>
26. Lavina B, Dera P, Downs RT, Yang W, Sinogeikin S, Meng Y, Shen G, Schiferl D (2010) Structure of siderite FeCO₃ to 56 GPa and hysteresis of its spin-pairing transition. *Phys Rev B* 82(6): 064110. <https://doi.org/10.1103/PhysRevB.82.064110>
27. Ponomar VP, Dudchenko NO, Brik AB (2018) Synthesis of magnetite powder from the mixture consisting of siderite and hematite iron ores. *Minerals Eng* 122:277–284. <https://doi.org/10.1016/j.mineng.2018.04.018>
28. Sun Y, Han Y, Wei X, Gao P (2016) Non-isothermal reduction kinetics of oolitic iron ore in ore/coal mixture. *J Thermal Anal Calorimetry*. <https://doi.org/10.1007/s10973-015-4863-y>
29. Budrugaec P, Petre AL, Segal E (1996) Some problems concerning the evaluation of non-isothermal kinetic parameters: solid-gas decompositions from thermogravimetric data. *J Thermal Anal Calorimetry* 47(1):123–134. <https://doi.org/10.1007/bf01982692>
30. Škvára F, Šesták J (1975) Computer calculation of the mechanism and associated kinetic data using a non-isothermal integral method. *J Thermal Anal Calorimetry* 8(3):477–489. <https://doi.org/10.1007/BF01910127>
31. Yu J, Han Y, Li Y, Gao P, Li W (2017) Mechanism and kinetics of the reduction of hematite to magnetite with CO–CO₂ in a micro-fluidized bed. *Minerals* 7(11):209
32. Dhupe A, Gokarn A (1990) Studies in the thermal decomposition of natural siderites in the presence of air. *Int J Mineral Process* 28(3–4):209–220. [https://doi.org/10.1016/0301-7516\(90\)90043-X](https://doi.org/10.1016/0301-7516(90)90043-X)
33. Van Siclen CD (1996) Random nucleation and growth kinetics. *Phys Rev B* 54(17):11845–11848. <https://doi.org/10.1103/PhysRevB.54.11845>
34. Zhang Q, Sun Y, Han Y, Li Y, Gao P (2020) Effect of thermal oxidation pretreatment on the magnetization roasting and separation of refractory iron ore. *Mineral Process Extractive Metallurgy Rev*. <https://doi.org/10.1080/08827508.2020.1837126>

Publisher's Note Springer Nature remains neutral with regard to jurisdictional claims in published maps and institutional affiliations.